Chapter 4 *Structure and Magnetization reversal along with bipolar switching in nanoparticles of $CeCr_{1-x}Fe_xO_3$ ($0.06 \leq x \leq 0.1$).*

4.1 Introduction

In this chapter, we have investigated the structural, magnetic, and bipolar switching properties of $CeCr_{1-x}Fe_xO_3$ ($0.6 \leq x \leq 0.1$) nanoparticles synthesized using a one-step solution combustion method. Structural and Raman analyses shows an increase in the distortion of the orthorhombic structure after substituting Fe^{3+} ions, due to the rotation/tilting of Cr-O_6 octahedra, which is discussed in detail in sections 4.2 and 4.3. The Néel transition, T_{N2}, decreases from ~260 K at x = 0 to 245 K at x = 0.1 due to the dilution of Cr^{3+}-O-Cr^{3+} antiferromagnetic interaction. Below the Néel transitions, we have observed some interesting magnetic features, such as the compensation temperature, T_{comp}, and spin reorientation temperature, T_{SR}, which are discussed in detail in section 4.4.1. In section 4.4.2, we analyzed the negative magnetization data for x = 0 and 0.06, which shows magnetization reversal. Most importantly, we demonstrate a stable bipolar switching of magnetization by varying the external field for x = 0.06, which could be exploited for its potential use in data storage and magnetic switching-based nonvolatile magnetic memory devices, as discussed in section 4.4.3. All the important findings are summarized in section 4.5.

4.2 Structure and microstructure

4.2.1 Structural analysis

Figure 4.1 depicts the XRD pattern at room temperature of $CeCr_{1-x}Fe_xO_3$ ($0 \leq x \leq 0.1$). All the peaks are well resolved and are indexed based on an orthorhombic distorted perovskite structure with the space group *Pnma* (no. 62). No impurity phase is observed in the XRD patterns.

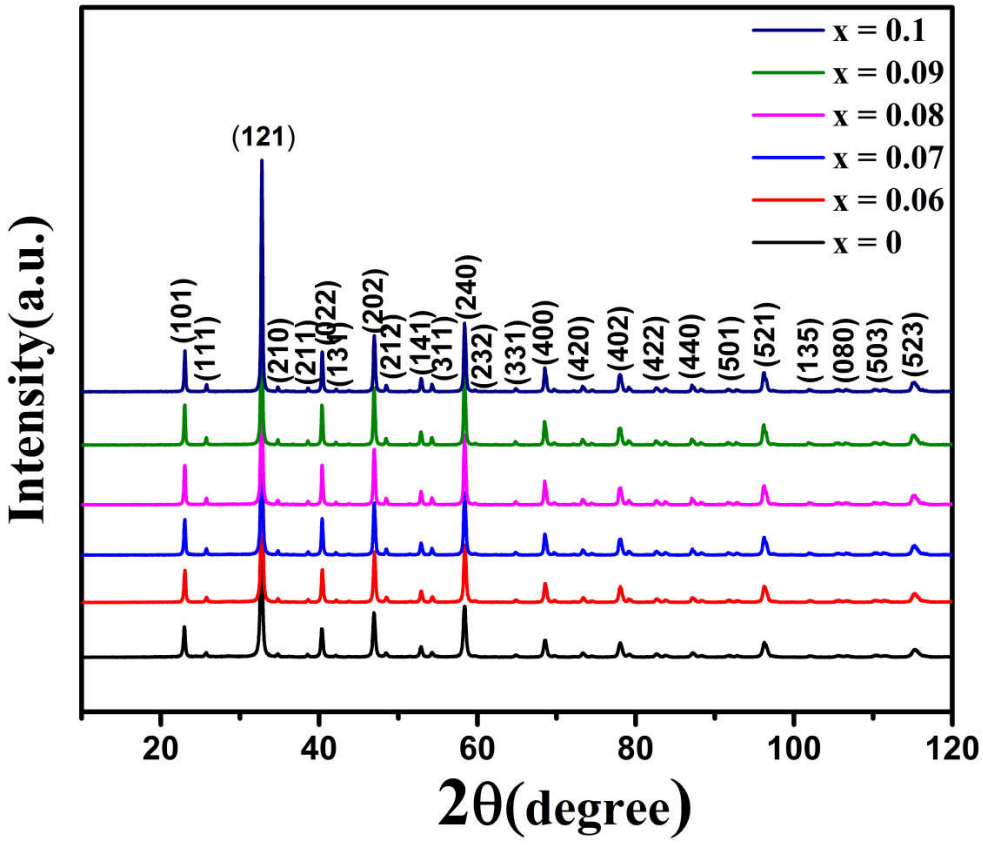

Figure 4.1 X-ray diffraction pattern of $CeCr_{1-x}Fe_xO_3$ ($0.0 \leq x \leq 0.1$).

Further, we have refined XRD spectra to determine the structural parameters. Taking Pseudo-Voigt as peak profile function, the Rietveld refinement of the $CeCr_{1-x}Fe_xO_3$($0 \leq x \leq 0.1$) samples are carried out and are shown in figure. 4.2(a-f). The experimental, calculated, and their difference patterns are denoted as a solid line, dot, and continuous bottom line, respectively. The position of Bragg reflections represented by the tick marks above the difference pattern indicates the reflection planes of the orthorhombic phase.

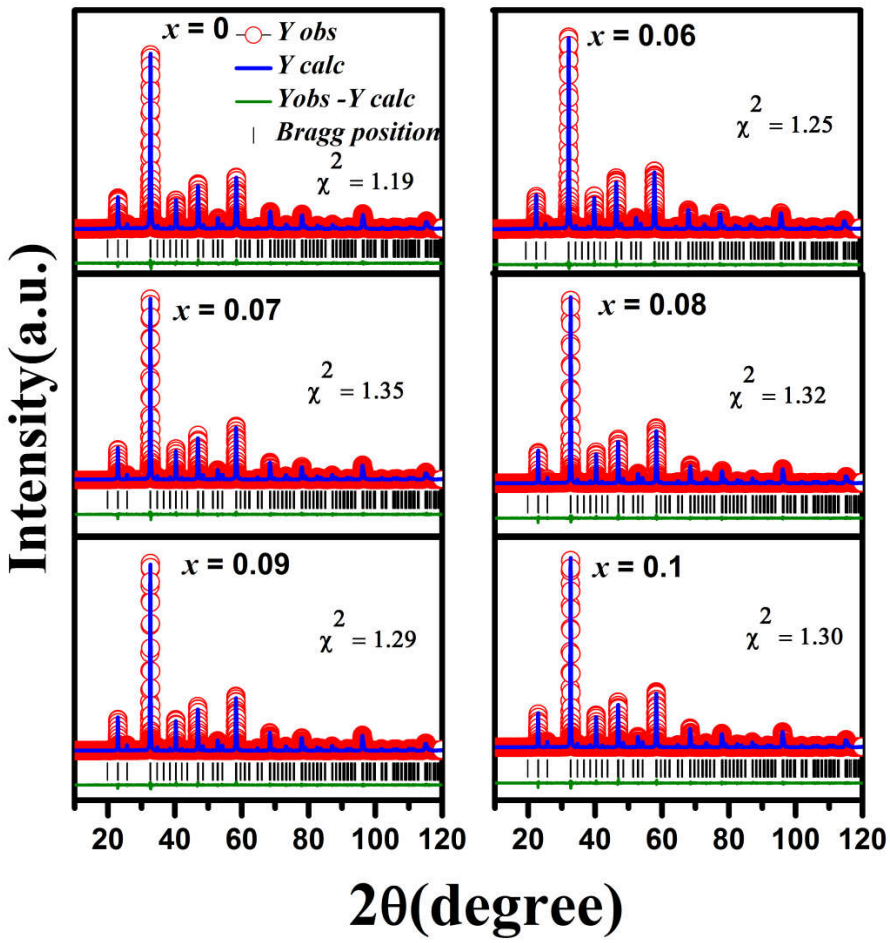

Figure 4.2 Experimental and Rietveld refined XRD patterns along with the difference between observed and calculated patterns of $CeCr_{1-x}Fe_xO_3$ ($0 \leq x \leq 0.1$).

Table 4.1 Structural parameter calculated from Rietveld refinement of XRD pattern.

Compound	***x* = 0**	***x* = 0.06**	***x* = 0.07**	***x* = 0.08**	***x* = 0.09**	***x* = 0.1**
A	5.4743(3)	5.4797(2)	5.4817(2)	5.4820(2)	5.4837(2)	5.4837(2)
B	7.7340(3)	7.7382(3)	7.7384(2)	7.7395(2)	7.7411(2)	7.7417(2)
C	5.4802(3)	5.4828(2)	5.4835(2)	5.4844(2)	5.4852(2)	5.4857(2)
V	232.02	232.487	232.607	232.698	232.852	232.888
a_P	3.0171	3.0744	3.0750	3.0753	3.0760	3.0762
Ce						
X	0.0273(1)	0.0290(1)	0.0292(1)	0.0293(1)	0.0295(1)	0.0293(1)
Y	0.25000	0.25	0.25	0.25	0.25	0.25
Z	-0.0066(2)	-0.0062(3)	-0.0061(3)	-0.0065(2)	-0.0064(2)	-0.0065(2)
B_{iso}(Å^2)	0.134	0.134	0.134	0.134	0.134	0.134
Cr/Fe						
X	0.00	0	0	0	0	0
Y	0.00	0	0	0	0	0
Z	0.50	0.5	0.5	0.5	0.5	0.5
B_{iso}(Å^2)$_{Cr}$	0.233	0.233	0.233	0.233	0.233	0.233
B_{iso}(Å^2)$_{Fe}$	-	0.232	0.232	0.232	0.232	0.232
O1						
X	0.4878(14)	0.4930(16)	0.4857(16)	0.4878(15)	0.4875(14)	0.4848(15)
Y	0.25000	0.25	0.25	0.25	0.25	0.25
Z	0.075(2)	0.075(3)	0.070(2)	0.070(2)	0.076(2)	0.072(2)
B_{iso}(Å^2)	0.450	0.450	0.450	0.450	0.450	0.450
O2						
X	0.281(2)	0.280(3)	0.283(2)	0.283(2)	0.280(2)	0.286(2)
Y	0.0333(14)	0.0325(14)	0.0372(12)	0.0353(11)	0.0353(11)	0.0347(12)
Z	0.720(2)	0.712(2)	0.718(2)	0.715(2)	0.7147(20)	0.719(2)
B_{iso}(Å^2)	0.450	0.450	0.450	0.450	0.450	0.450
U	0.177	0.112	0.050	0.039	0.037	0.036
V	-0.069	-0.050	-0.012	-0.009	-0.011	-0.008
W	0.075	0.058	0.042	0.034	0.031	0.031
Cr(Fe)-O1-Cr(Fe)	155.69(9)	155.90(14)	157.10(9)	157.23(9)	155.37(10)	156.44(9)
Cr(Fe)-O2-Cr(Fe)	159.5(5)	158.7(6)	157.7(4)	157.8(4)	158.2(4)	158.2(4)
Cr(Fe)-O1	1.978(2)	1.978(3)	1.974(2)	1.974(2)	1.981(2)	1.977(2)
Cr(Fe)-O2	1.971(11)	1.941(15)	1.980(11)	1.968(11)	1.954(11)	1.994(11)
Cr(Fe)-O2’	1.964(11)	2.002(13)	1.972(11)	1.983(11)	1.995(11)	1.956(11)
<Cr-O>	1.971	1.974	1.975	1.975	1.976	1.976
<Ce-O>	2.571	2.553	2.548	2.551	2.546	2.548
‘t’	0.923	0.915	0.912	0.913	0.910	0.912
Φ[010]	6.99	7.80	7.74	7.75	7.46	7.65
Θ[101]	12.15	12.05	11.45	11.39	12.16	11.78

Theoretically, presuming Fe^{3+}substituting the Cr^{3+} site, one can estimate the distorted orthorhombic site average ionic radii, R_{avg} as per the given equation $R_{avg} = (x \times (R_{Fe}^{3+})^2 + (1-x) \times (R_{Cr}^{3+})^2)^{1/2}$, where $R_{Cr}^{3+}$and R_{Fe}^{3+} are 0.615 Å and 0.645 Å, respectively. The estimated R_{avg} for each composition is provided in Table 4.1. The pseudo-cubic lattice parameter calculated from orthorhombic unit cell volume using relation $a_P = V^{1/3}/2$ is found to be increased with an increase in *x*.

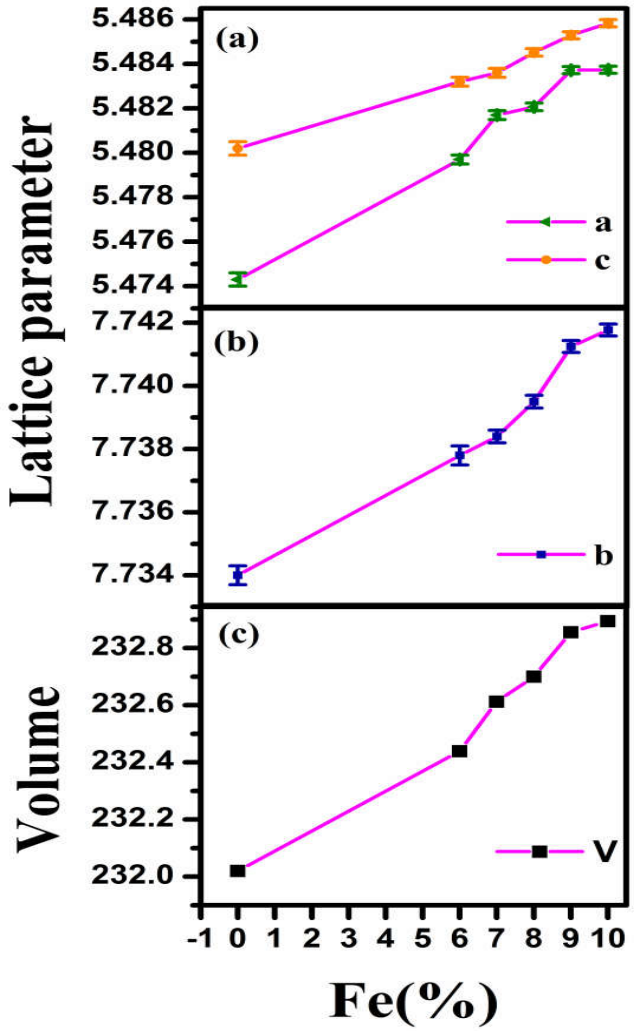

Figure 4.3 The extracted lattice parameter and volume of $CeCr_{1-x}Fe_xO_3$ ($0 \leq x \leq 0.1$) from Rietveld refinement.

The changes in bond angles of Cr–O1–Cr and Cr-O2-Cr with *x* are plotted in figure. 4.5(a). It may be noted that with increase in *x* from 0 to 0.08, the bond angle, Cr–O1–Cr increases followed by a significant decrease at *x* = 0.09. It may be noted that with increase in *x* from 0 to 0.08, while the bond angle, Cr–O1–Cr increases followed by a significant decrease at *x* = 0.09, Cr-O2-Cr shows the opposite trend. With increase in *x*, deviation in both apical and equatorial bond lengths occurs. From the Table.1, we have observed that Cr-O1 bond length decreases up to *x* = 0.08 and increases at *x* = 0.09 while in case of equatorial, bond length Cr-O2 increases up to *x* = 0.08 and decreases at *x* = 0.09. In general, the bond lengths and bond angles are correlated to each other as reported by Yamanka et al. and Gillspie et al. [119,120]. While <Cr-O> bond length after Fe^{3+} incorporation is found to increase, the <Ce-O> bond length in fact decreases. The expected distortion in $CeCrO_3$ structure determined from the Goldschmidt tolerance factor *t*, where $t = <Ce\text{-}O>/\{\sqrt{2}(<Cr-O>)\}$, is found to be 0.923 for *x* = 0 and decreases to 0.912 when *x* = 0.1 without any significant variation in *t* for the intermediate compositions. Evidently, the decrease in the tolerance factor suggests that the Fe substitution in $CeCrO_3$ lattice leads to more distortion in orthorhombic structure. The Williamson–Hall method is used to separate the crystallite size and lattice strain of the XRD line broadening. According to this method, *x*-ray diffraction peak broadening $\beta_{hkl} = \beta_{size} + \beta_{strain}$. The actual peak broadening (β) is obtained by correcting the experimental peak broadening (β_{exp}) and the instrumental broadening (βins) as $\beta_{hkl}^2 = \beta_{exp}^2 - \beta_{ins}^2$. β_{ins} is the broadening due to the instrument, where β_{ins} was obtained from the silicon powder standard using the angular dependence proposed by Caglioti et al. acoording to equation [110,111]:

$$\beta_{ins} = \sqrt{Utan^2\theta + Vtan\theta + W} \quad [4.1]$$

Hence, XRD peak broadening $\beta_{hkl} = \beta_{size} + \beta_{strain}$ equation can be in modified form as:

$$\beta_{hkl} = \frac{0.9\lambda}{Dcos\theta} + 4\varepsilon\, tan\theta \quad [4.2]$$

$$\beta_{hkl}cos\theta = \frac{0.9\lambda}{D} + 4\varepsilon\, sin\theta \quad [4.3]$$

where β_{hkl} is peak broadening, λ is wavelength of Cu-Kα radiation (λ = 1.5406 Å), ε is strain, and D is crystallite size. In general, a plot drawn between βcosθ and 4sinθ (straight line expected) allows one to extract the particle size and lattice strain from its intercept and slope, respectively (figure 4.4). Calculated crystallite size from Williamson-Hall method shows that with substitution of Fe from *x* = 0 to 0.1, the crystallite size increases from 36.3 to 45.5 nm (Figure 4.5 (b)). The strain also increase from 9.55×10^{-4} to $11.3\times10^{-4}$with increase in *x* from 0 to 0.1 fallowed by a decrease at *x* = 0.09 (figure 4.5(b)).The increase in crystallite size can be attributed to the larger ionic radii of Fe^{3+}(0.645Å) compared to Cr^{3+}(0.615Å).

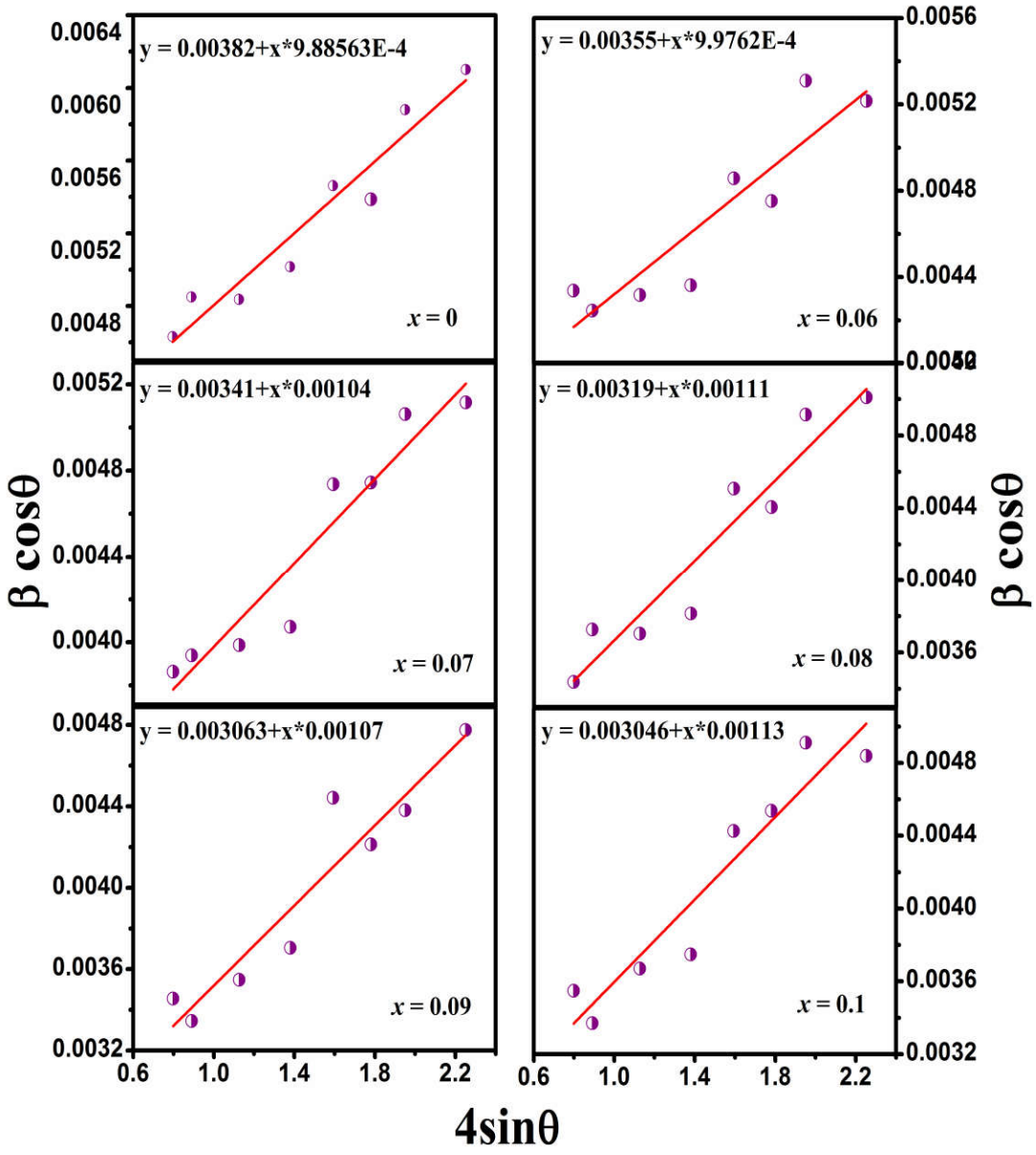

Figure 4.4 Williamson-Hall plot for $CeCr_{1-x}Fe_xO_3$ ($0 \leq x \leq 0.1$).

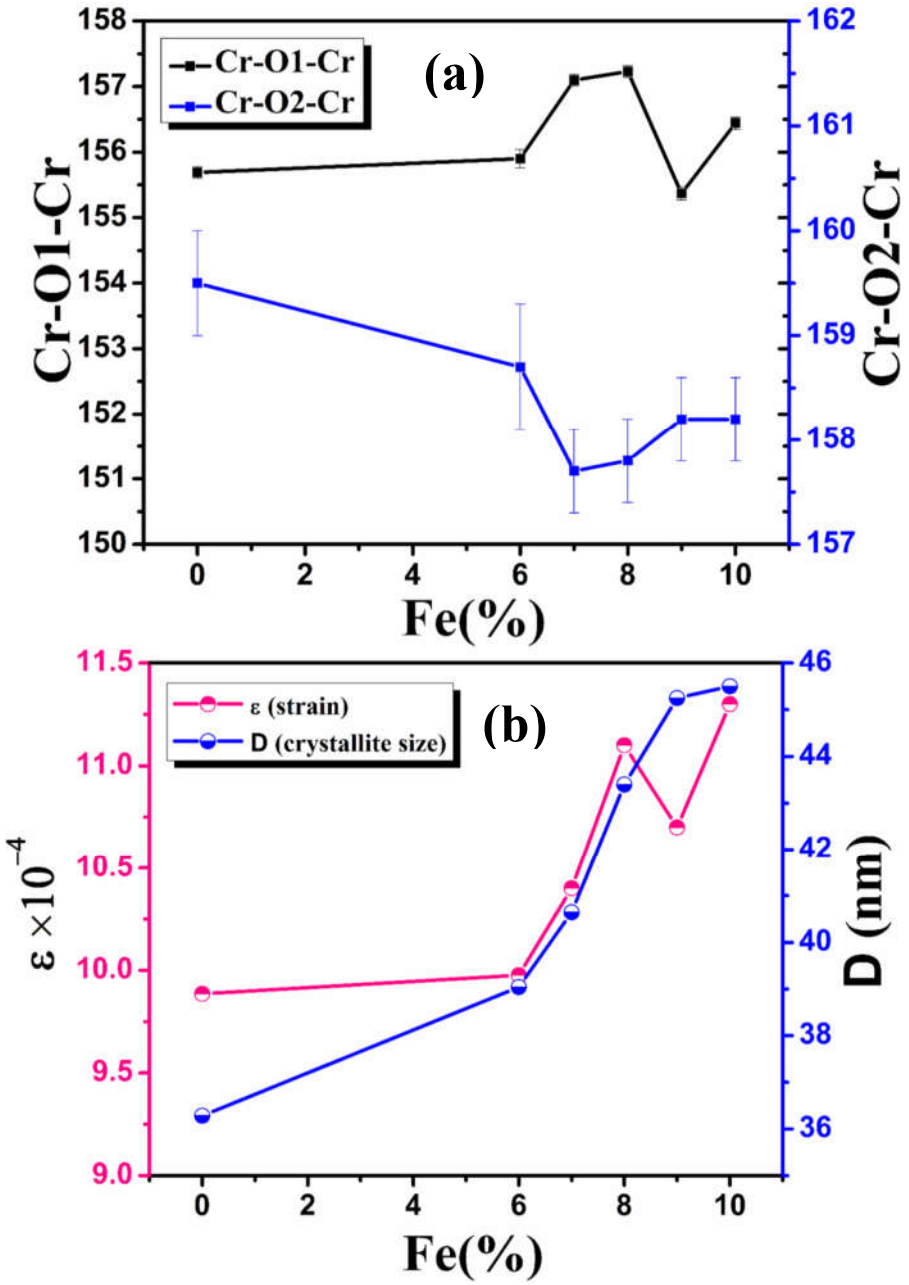

Figure 4.5 (a) Variation in bond angle Cr-O1-Cr and Cr-O2-Cr with Fe concentration calculated from Rietveld refinement. (b) Variation in crystallite size and strain with Fe concentration calculated from using Williamson-Hall plot

4.2.2 Microstructural and elemental analysis

Typical transmission electron micrograph depicted in figure.4.6(a) demonstrates the agglomerated particles of semispherical shape. The particle size distribution histogram reveals that the average particle size is found to be of~ 50 nm for $x = 0.08$ as shown in figure 4.6(b).

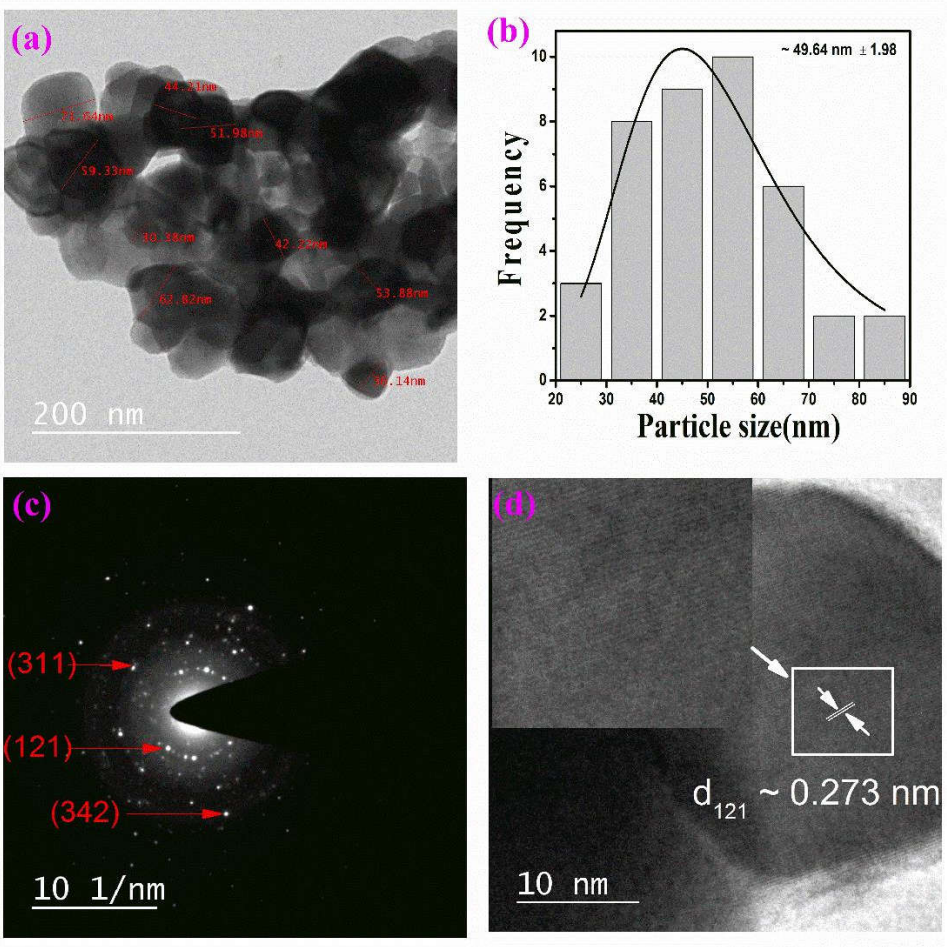

Figure 4.6 TEM and HRTEM image of $x = 0.08$ and SEAD pattern.

The TEM result is consistent with the calculated crystallite size from Debye-Scherrer formula. HRTEM confirms the interplanar spacing (d) as 0.2738 nm corresponding to (121) of orthorhombic phase (Figure4.6(c)). EDAX analysis shows that the ratio of metal in compounds is close to RE: Cr/(Cr+Fe) = 1: 1, which is an ideal composition for metal in the perovskite structure. EDAX patterns of $CeCr_{1-x}Fe_xO_3$ are shown in figure 4.7 and the elemental analysis data added in Table 4.2 demonstrates that concentration of Fe is in good agreement with stoichiometric composition.

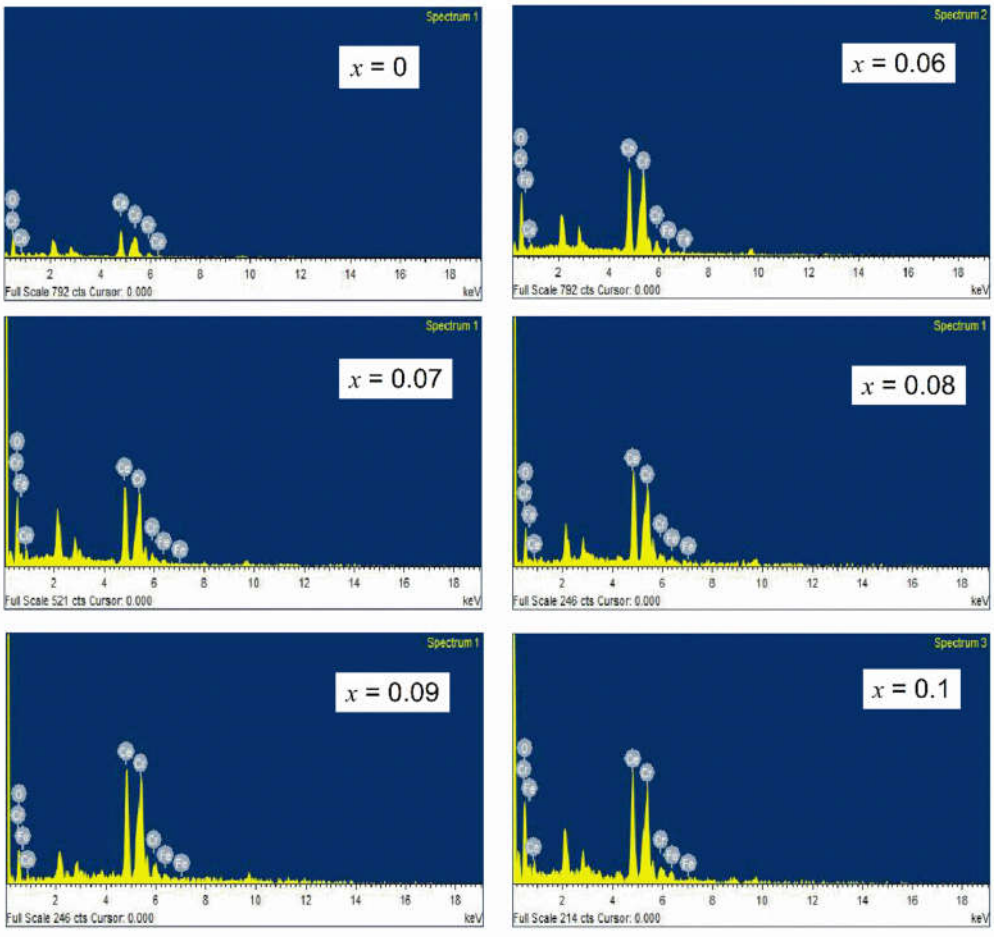

Figure 4.7 EDAX mapping image of $CeCr_{1-x}Fe_xO_3$ ($0 \leq x \leq 0.1$).

Table 4.2 Data obtained from EDAX for Fe in $CeCr_{1-x}Fe_xO_3$ ($0 \leq x \leq 0.1$).

Composoition '*x*'	Ce atomic%	Fe Atomic%	Cr Atomic%
0	18.88	-	18.74
0.06	22.44	1.53	21.76
0.07	20.42	1.85	19.03
0.08	21.13	1.85	18.89
0.09	30.97	3.41	26.26
0.1	19.78	2.25	18.20

4.3 Raman Analysis

The room temperature Raman spectra of $CeCr_{1-x}Fe_xO_3$ ($0 \leq x \leq 0.1$) are shown in figure. 4.8. Here we observe five Raman modes present within 100–750 cm^{-1} for the orthorhombic Pnma $CeCrO_3$ perovskite. The other modes are either too weak in intensity or have energies below the experimental cut-off wave number. The observed peaks at 350.1, 352.3,408.7,450.5, and 543 cm^{-1} are corresponding to $A_g(5)$, $B_{1g}(2)$, $B_{2g}(3)$, $A_g(6)$, and $B_{3g}(3)$ modes, respectively. The peaks marked with '*' are the fluctuation in data point. It is well established that in a orthorhombic structure of perovskite, Raman modes is associated with the corresponding activated distortion due to special atomic motion such as rotation of CrO_6 octahedra, antisymmetric stretching vibrations of the O2 and O1, vibration of Ce-O etc. [108,112,121]. $A_g(5)$ mode arises due to the out of phase rotation of CrO_6 octahedra around x-axis depending upon the octahedral tilting [108,121]. $B_{1g}(2)$ mode belongs to the symmetry involve mode-mixing and crossing [121]. The $A_g(6)$ and $B_{2g}(3)$ modes are related to the bending of the CrO_6 octahedra while as $B_{3g}(3)$mode corresponds to the antisymmetric stretching vibrations of the O2 and

O1 atoms [108,112]. Further, it has been reported that the A_g and B_g modes vary linearly with increasing ionic radii of $R^{3+}$and also with octahedra tilting [108].

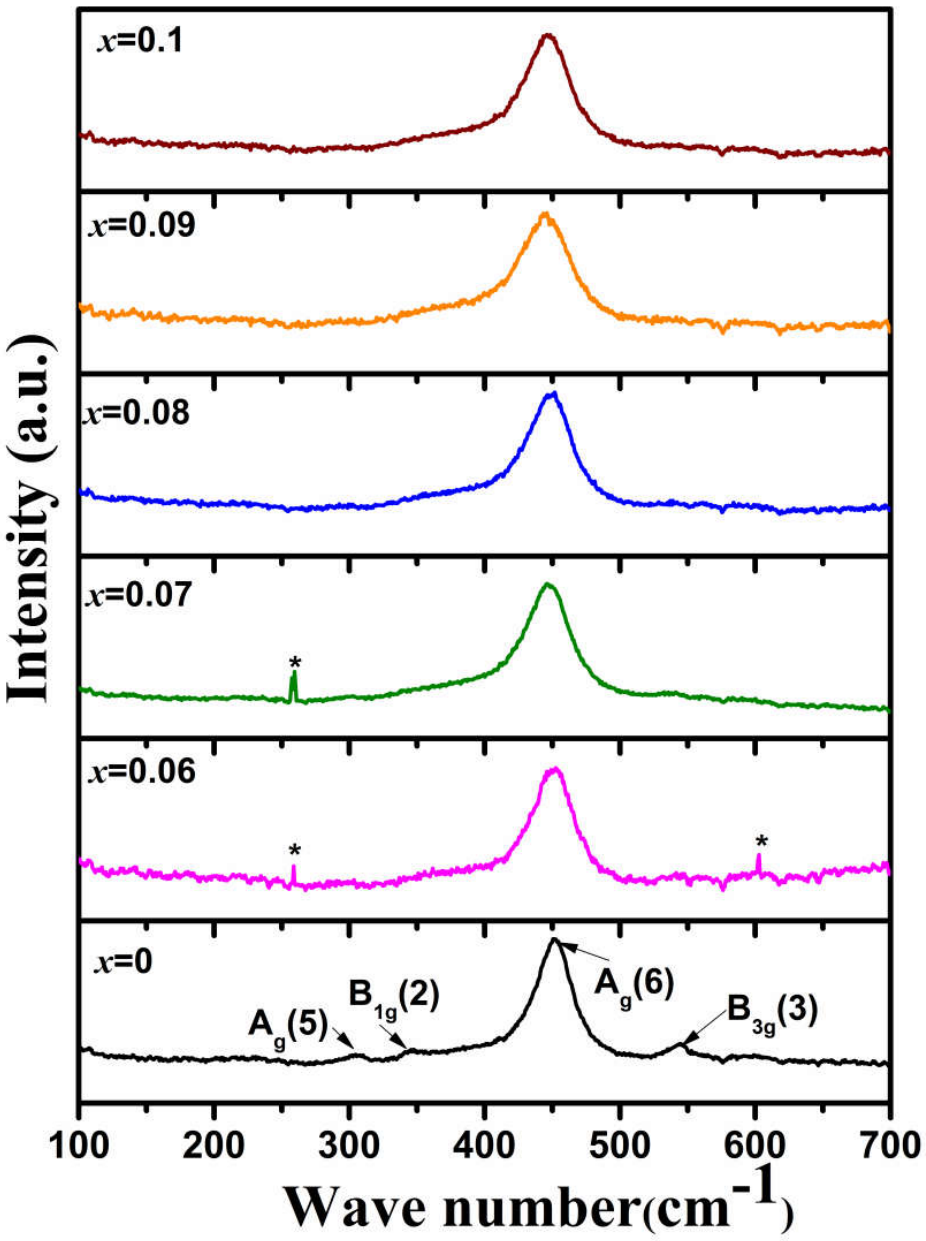

Figure 4.8 Raman spectra of $CeCr_{1-x}Fe_xO_3$ ($0 \leq x \leq 0.1$) recorded at room temperature (the peaks marked with '*' are fluctuation in data point).

We observe that with increasing *x*, the phonon frequency of the A_g (6) mode changes from ~450.5cm^{-1}(*x* = 0) to ~446.35 (*x* = 0.1) cm^{-1} with a respective change in tilt angle i.e. ϕ[010] [112]. In Raman scattering, the frequencies of specific lattice irrational modes are related to structural distortion. This is not hard to understand that the A_g (6) mode are associated with the bending of the CrO_6 octahedra, which results in the rotation of the CrO_6 octahedra in [010] plane [108,112]. Thus, the rotation leads to a change in the octahedral tilt angle, ϕ. In general, $RCrO_3$ crystallizes in an orthorhombically distorted perovskite structure with space group, Pnma. Orthorhombic Pnma structure is obtained from an ideal cubic Pm3m perovskite structure, by an antiphase tilt of the adjacent CrO_6 octahedra ($a^-b^+a^-$). The distortion in perovskite structure is contributed either due to the co-operative tilting of octahedra or due to the Jahn-Teller active element. In $CeCr_{1-x}Fe_xO_3$, since $Cr^{3+}$and $Fe^{3+}$are Jahn-Teller (JT) inactive cations, leading to almost no dispersion in the Cr-O bonds, the distortion can only be contributed from the co-operative tilting of octahedra. Further, we have calculated θ and ϕ using the equation given below as formulated previously [108,109]

$$\theta = \arctan\left[4 \times \frac{\sqrt{w_{O(1)}^2 + u_{O(1)}^2}}{b}\right] \qquad [4.2]$$

$$\phi = \arctan\left[4 \times \frac{\sqrt{w_{o(2)}^2 + u_{o(2)}^2}}{\sqrt{c^2 + a^2}}\right] \qquad [4.3]$$

Where '*w'* and '*u*' are the atomic displacement (in Å) of O1 and O2 atoms. θ and ϕ describe octahedral rotations around the [101] and [010] axes, respectively. θ and ϕ for all the compounds are listed in Table.4.1. While tilt angle, θ decreases from 12.16° to 11.78° when x varies from 0 to 0.1, the tilting angle, ϕ increases from 6.99° to 7.45°. The decrease in θ and increase in ϕ can be attributed to the deviation of deviation of apical oxygen (O1) and planer oxygen (O2) from its special position. After substitution of Fe, apical oxygen O1 from its special position (i.e. along x it is 0.50 and along z-axis, it is 0.00) is in such a way that $\sqrt{(w_{O(1)}^2 + u_{O(1)}^2)}$ which is directly proportional to θ reduces from 0.4164 Å for x = 0 to 0.4036 Å for x = 0.1. Whereas the planer oxygen O2 deviate from its special position (i.e. along x is 0.25 and along z is 0.75) in such a way that $\sqrt{(w_{O(2)}^2 + u_{O(2)}^2)}$ which is directly proportional to ϕ increases from 0.4861 Å for x = 0 to 0.5105 Å for x = 0.1. Such changes in θ and ϕ are well corroborated with the change observed in A_g (6) mode (figure 4.9). Thus, after substitution of Fe, the decrease in intensity of all other modes and increase in Ag(6) mode could be understood from the tilt angle, ϕ. The increase in tilt angle associated with the bending of CrO_6 octahedra (ϕ), therefore shows an increase intensity of Ag(6) Raman mode as observed in the present case. Hence, we confirm a weak distortion of CrO_6 octahedra from both XRD and Raman spectra.

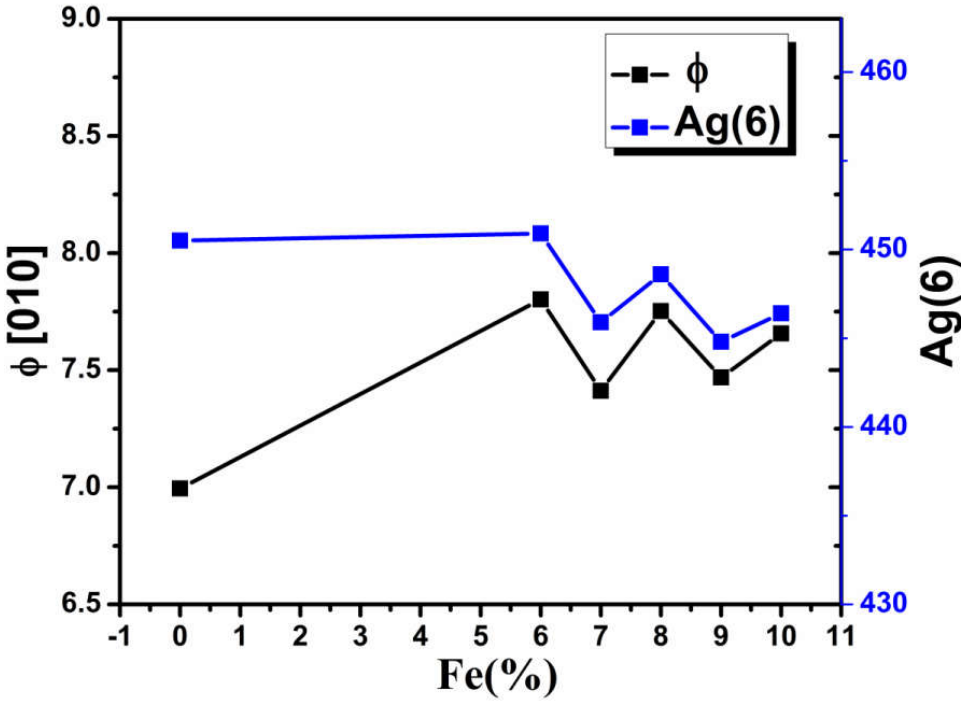

Figure 4.9 Variation of Ag(6) mode and tilt angle ϕ[010] with Fe concentration

4.4 Magnetic properties

4.4.1 Temperature dependent magnetization

Zero field cooled (*ZFC*) and field cooled (*FC*) magnetization measured with varying temperature for $CeCr_{1-x}Fe_xO_3$ ($0 \leq x \leq 0.1$) are depicted in figure 4.10. The magnetization curve recorded in *ZFC* and *FC* mode for pristine $CeCrO_3$ at 0.5 kOe shows a paramagnetic to an antiferromagnetic transition, T_N at around 260 K (figure 4.10(a)). Below T_N, M_{FC} (Field cooled magnetization) increases showing a maximum magnetization at a temperature, T_{max} at ~ 217 K. With further decreasing the temperature, M_{FC} decreases monotonously and

intersects the zero-magnetization axis at a temperature known as compensation temperature (T_{comp}) which is observed at 58 K.

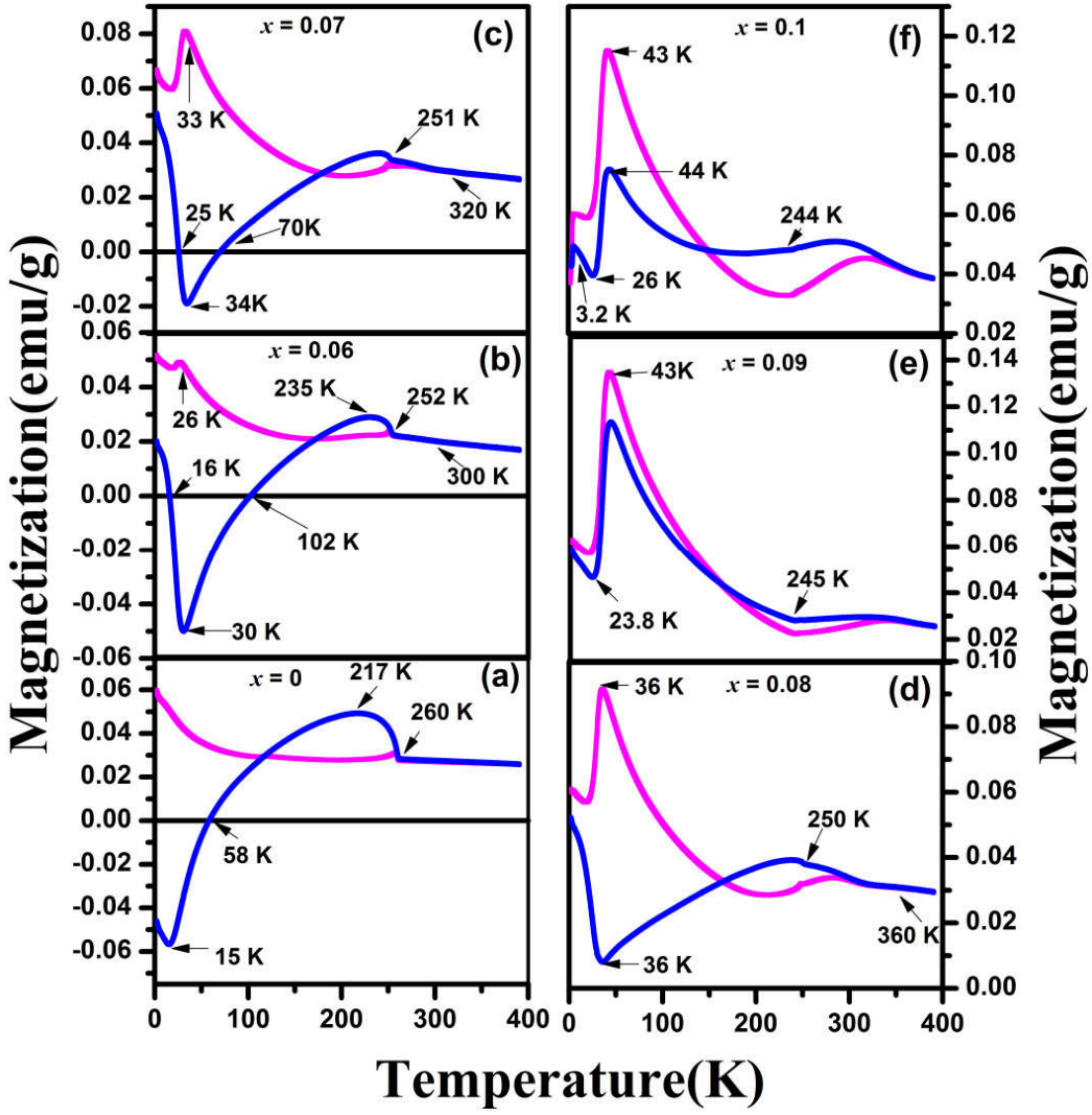

Figure 4.10 Temperature dependent magnetization of $CeCr_{1-x}Fe_xO_3$ ($0 \le x \le 0.1$) in ZFC and FC mode under 500 Oe external field. (Blue solid line represents FC magnetization and magenta solid line represents ZFC magnetization)

For the nanoparticles similar T_{comp} has also been reported by *Shukla et al.* and *Taheri et al.* at low external applied field [90,91]. Thereafter, we observe a negative magnetization which approaches a maximum magnitude of 0.0568 emu/g at a temperature known as spin reorientation transition, T_{SR} at 15 K followed by an increase in magnetization up to 2 K. It is observed for M_{FC} in x = 0.06 that in addition to a weak magnetic ordering at around T_{N1} ~ 300 K, an abrupt increase in M_{FC} is observed at T_{N2} ~ 253 K (figure 4.10(b)). While T_{N1} is ascribed to Cr^{3+}-O-Fe^{3+} ordering, Cr^{3+}-O-Cr^{3+} ordering is represented by T_{N2}. Further with decreasing temperature, showing a maximum magnetization at ~ 235 K, M_{FC} decreases monotonously and crosses the M_{ZFC} at T_{cross}~ 172 K. M_{FC} keeps on decreasing and the T_{comp} is observed at ~ 102 K. Afterwards, M_{FC} reaches a maximum negative magnetization of -0.049 emu/gat T_{SR} ~ 30 K. Below T_{SR}, the magnetization increases again and crosses zero magnetization at T_{comp2} ~ 16 K. Eventually, M_{FC} attains a positive magnetization below 16 K and continues to increase up to 2 K. M_{FC} at 2 K attains 0.020 emu/g. With an increase in 'x' to 0.07, the transition temperature such as T_{N1}, T_{N2}, T_{cross}, T_{comp1}, T_{SR} and T_{comp2} are modified. For instance, T_{N1}, T_{cross}, T_{SR}, T_{comp2} increases to ~ 320, 179, 34 and 25 K, respectively, whereas T_{N2} and T_{comp1} decreases to 251 and 70 K, respectively. M_{FC} attains a maximum negative magnetization of 0.01908 emu/g at T_{SR} ~ 34 K which is almost 2.5 times less than that observed for x = 0.06. The magnetization at 2 K is found to be ~ 0.05084 emu/g which is also approximately 2.5 times the M_{FC} at 2 K of x = 0.06. It is important to mention that though T_{SR} increases, maximum negative magnetization at T_{SR} is drastically decreased and M_{FC} is significantly increased at 2 K. Further, increasing x to 0.08, while the magnetic ordering, T_{N1} increases to ~ 360 K, T_{N2} decreases to ~ 250 K. The magnetic ordering at T_{N2} in x = 0.08 is weak compared to x = 0.06 and 0.07. Below T_{N2}, the total magnetization

becomes positive and results in the absence of compensation of magnetization along with a decrease in T_{cross} to 164 K. The minimum magnetization at T_{SR} observed at 35 K becomes positive showing a M_{min} of ~ 0.008 emu/g. Further increasing x to 0.09, while a significant increase in T_{N1} to 390 K is observed, T_{N2} decreases to 245 K. This is evidenced from a kink depicted in the dM/dT plot (shown figure 4.11). Below T_{N2}, both M_{FC} and M_{ZFC} increases and show a peak at T_{SR} ~ 43 K. Surprisingly, we observe a new spin reorientation at ~ 24 K followed by an increase up to 2 K. Finally, when x is 0.1, the magnetic ordering, T_{N1} reaches 390 K without any significant change in T_{N2}. Below T_{N2}, M_{FC} and M_{ZFC} crosses at ~ 148 K which is less than the T_{cross} of rest of the compositions. The M_{FC} and M_{ZFC} are found to be positive and increases up to T_{SR1} ~ 44 K. Below T_{SR1}, two new spin reorientations are observed at ~26 K and 3.2 K. Here we conclude that with incorporation Fe in $CeCrO_3$ nanoparticles, we observe a few new findings such as increase in T_{SR}, compensation of magnetization, and more complex magnetic transitions like many spin reorientations when x > 0.08.

In $CeCrO_3$ nanocrystalline particles, the observed magnetic anomalies such as T_N, T_{comp}, T_{SR} have been explained on the basis of competition between the interaction among Cr^{3+} and Ce^{3+} moments [90]. In FC measurement, below T_N (260 K), Cr^{3+} moments orders antiferromagnetically in the field direction imposing a local field upon the Ce^{3+} moments. Hence, the Ce^{3+} moments experience a local field, which is the superposition of the internal field due to the Cr^{3+} moments and the applied external field. The antiferromagnetic coupling between Ce^{3+} and the canted Cr^{3+} moments polarize the Ce^{3+} magnetic moments antiparallel with respect to ferromagnetic component of the Cr^{3+} moments. Hence, it results into a

compensation of magnetization and spin reorientation with decreasing temperature below T_N. When Fe^{3+} is substituted in $CeCrO_3$, the possible magnetic interactions are Cr^{3+}-O-Cr^{3+}, Cr^{3+}-O-Fe^{3+}, Fe^{3+}-O-Fe^{3+}, Ce^{3+}-O-Ce^{3+}, Ce^{3+}-O-(Cr^{3+}/ Fe^{3+}). In $CeCrO_3$, while Cr^{3+}-O-Cr^{3+} interaction takes place at $T_N \sim 260$ K, Ce^{3+}-O-Ce^{3+} interaction takes place below 15 K [90]. In $CeFeO_3$ however, Fe^{3+}-O-Fe^{3+} and Ce^{3+}-O-Ce^{3+} interaction takes place at ~ 645 K and ~ 1.8 K, respectively [92]. Ce^{3+}-O-Ce^{3+} ordering occurs at too low temperature and exhibits a short range ordering at higher temperature. However, replacing Cr^{3+} with Fe^{3+} in $CeCr_{1-x}Fe_xO_3$ (x = 0.06 to 0.1), Ce^{3+}-O-(Cr^{3+}/ Fe^{3+}) interaction plays an important role in different magnetic transitions below T_N. Therefore, it is reasonable to ascribe the magnetic transition T_{N1} to the Cr^{3+}-O-Fe^{3+} AFM ordering. It is observed that due to low concentration and random distribution, the interaction, Fe^{3+}-O-Fe^{3+} is very rare. Increasing x, the Cr^{3+}-O-Cr^{3+} interaction decreases at the expense of the Cr^{3+}-O-Fe^{3+} AFM interaction and leads to an increase in T_{N1}. T_{N1} increases monotonously from 300 K to above 390 K with increasing 'x' from 0.06 to 0.1. On the other hand, T_{N2} observed at 250 K when x = 0.06, does not vary significantly up to x = 0.08 and further decreases to 244 K when x is 0.1. Since the change n magnetization with temperature T_{N1} is sharp, therefore variation in T_{N1} with substitution of Fe^{3+} clearly visible from dM/dT v/s Temperature plot (figure 4.11). The change in magnetization with temperature is not sharp at T_{N2} due to nominal concentration of Fe. Therefore, the rate of change of magnetization with temperature is either constant or show small deviation from straight line. This is clearly observed in x = 0.06 and 0.07 where dM/dT is almost constant and above x = 0.07, there is a deviation from straight line. With the substitution of Fe^{3+} from x = 0 to 0.08, the decrease in T_{N2} can be attributed to decrease in Cr-O2-Cr super exchange angle from 159.5° to 157.8° while as increase in T_{N1} can be

attributed to increase in Cr-O1-Cr super exchange angle from 155.69° to 157.23°. At 0.09, T_{N1} increased to above room temperature although T_{N2} does not affected at all. It is also observed that M_{FC} of x = 0.09 shows an opposite behavior to that of M_{FC} of x = 0.08.

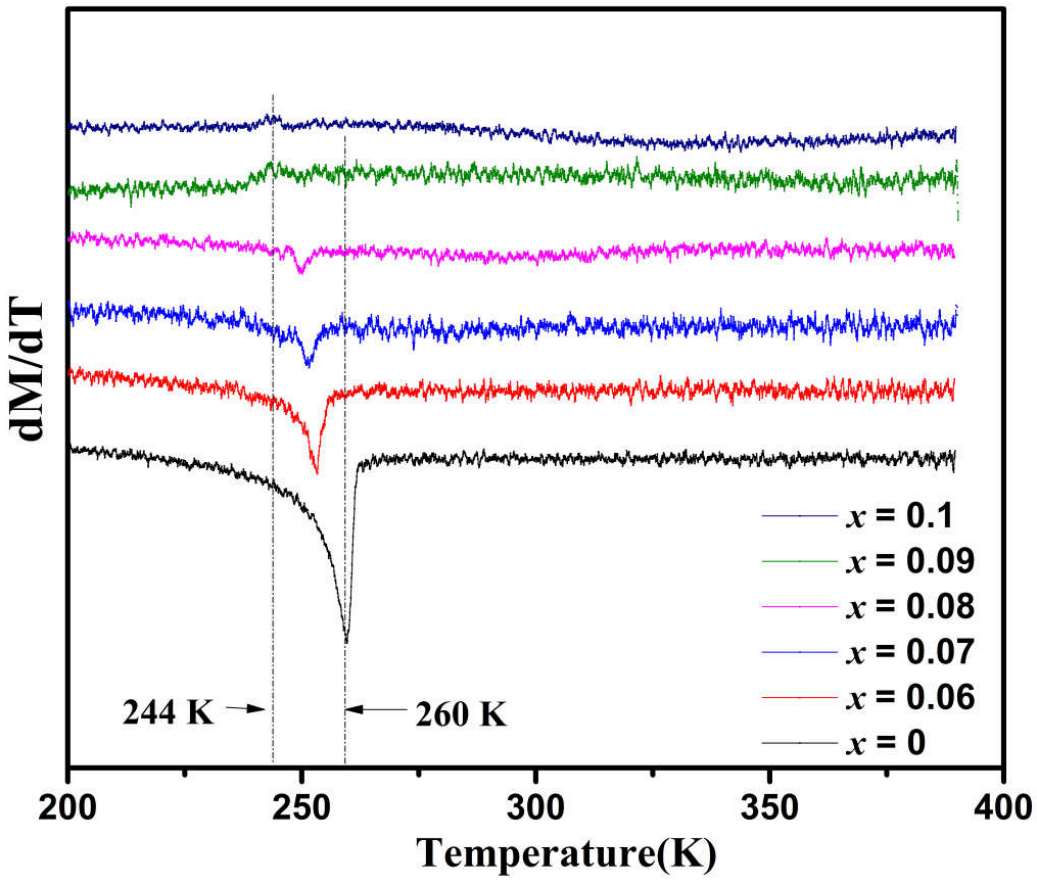

Figure 4.11 dM/dT v/s T plots of FC magnetization under 500 Oe for $CeCr_{1-x}Fe_xO_3$ ($0 \leq x \leq 0.1$).

Therefore, we can say that x = 0.09 is the critical concentration limit above which Cr^{3+}-O-Fe^{3+} interaction becomes predominant over the Cr^{3+}-O-Cr^{3+} interaction. At this concentration, decrease in Cr-O1-Cr bond angle to 155.37° and increase in Cr-O2-Cr bond angle to 158.2° can be said that the bond angle reset itself and now favoring the opposite interaction. With increasing x, a significant change in T_{comp} and T_{SR} are demonstrated (Figure 4.10). T_{SR} monotonously increases from 30 K to 44 K when x = 0.1. The superposition of

external field and internal field with decreasing temperature are important factor to govern the T_{comp} and T_{SR} in $RCrO_3$ system. When '*x*' increases from 0 to 0.06 the increase in T_{comp} and T_{SR} almost two fold also suggest an increase in internal field due to Cr^{3+}moment, can be attributed to increase in canted ferromagnetic moment of Cr^{3+} after Fe^{3+}substitution. Further, when *x* increases to 0.07 or above this concentration the substitution not affected the canting of Cr^{3+} but it diluted Cr^{3+}-O-Cr^{3+}interaction, as a result the internal field due to Cr^{3+} ions decreased (Figure 4.10). Similar results have been discussed by *Bora et al*. in Fe substituted $LaCrO_3$ [96]. The total field acting on the Ce^{3+} sublattice decreases compared to pristine $CeCrO_3$. Hence, T_{SR} increases with a decrease in T_{comp}. When x = 0.08, the external field overcomes the internal field and we observe a positive M_{FC} with an increase in T_{SR}. At x = 0.09 and 0.1, M_{FC} and M_{ZFC} remains same indicating the insignificant role of the internal field. T_{SR} increases without any compensation of magnetization. In addition, we observed several magnetic transitions besides another T_{SR} in x = 0.1 which needs to be understood.

4.4.2 Negative magnetization

The sign reversal of magnetization is further analyzed by fitting the FC magnetization curve between $T_{SR} < T < T_{max}$ using the following equation [57,74]:

$$M = M_{Cr} + \frac{C(H+H_I)}{(T-\theta_c)} \qquad [4.4]$$

Where M is the total magnetization, M_{Cr} is the magnetization due to the weak ferromagnetic component of canted Cr^{3+} moment, H_I is the internal magnetic field due to Cr^{3+}moment, C is the Curie constant, and θ_c is Weiss temperature. Figure 4.12 shows the fitting of *FC*

magnetization of $CeCr_{1-x}Fe_xO_3$ ($x = 0 \leq x \leq 0.07$) under 500 Oe and the evaluated parameters are given in Table 4.3.

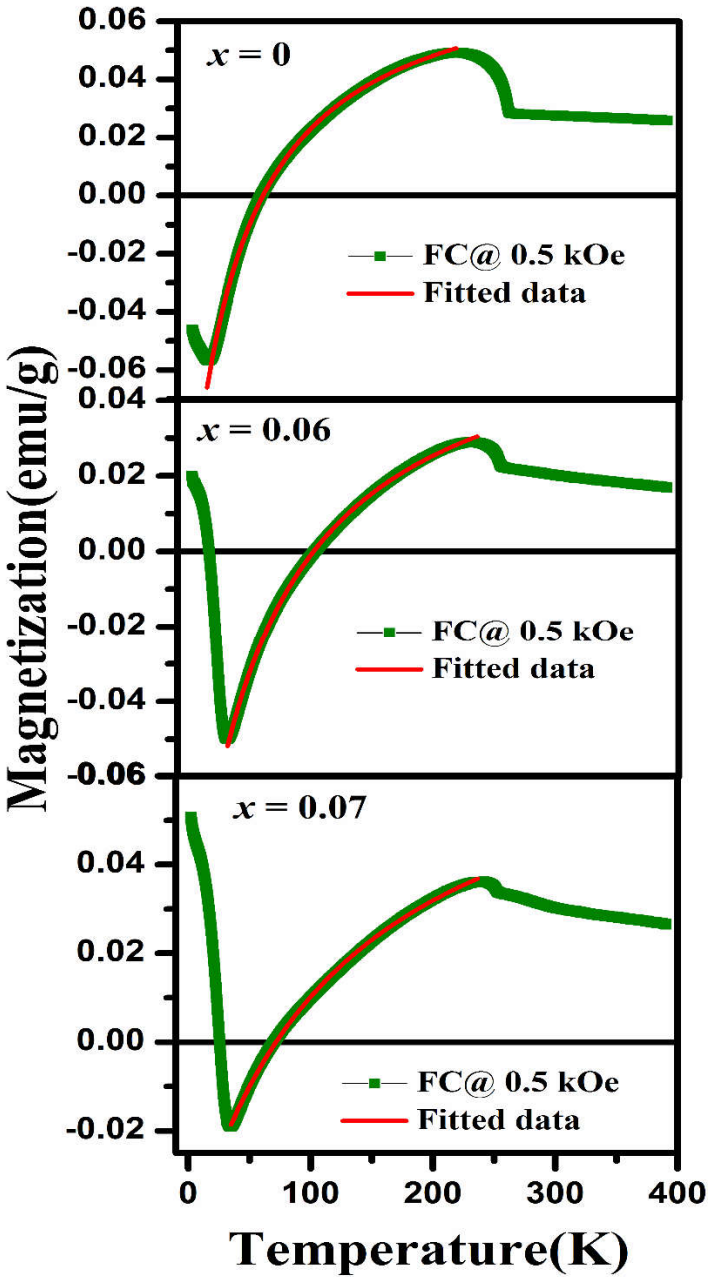

Figure 4.12 Fitting between T_{max} to T_{SR} of FC magnetization curve under 500 Oe of $CeCr_{1-x}Fe_xO_3$ (x =0, 0.06, 0.07) using equation-4.4.

The negative sign of H_I indicates the internal magnetic field direction due to Cr^{3+} ion which is in opposite direction to the applied magnetic field. As discussed before, here we find that when x increases from 0 to 0.06, H_I is found to increase from -939.48 to -1054.87 which can be attributed to increase in canting of Cr^{3+}moment after substitution of Fe^{3+}. Further with increasing x to 0.07 the internal field decreases due to dilution of Cr^{3+}-O-Cr^{3+} interaction. The θ_c's are found to be -43K, -60K and -122 K for x = 0, 0.06 and 0.07, respectively. The negative value of θ_c endorses the AFM interaction between the canted Cr^{3+} and Ce^{3+}/Ce^{3+}+Fe^{3+} moment in $CeCr_{1-x}Fe_xO_3$(x = 0, 0.06 and 0.07) under the application of low external magnetic field.

Table 4.3 Fitted parameter using equation 4.4 of M_{FC} curve $CeCr_{1-x}Fe_xO_3$ ($0 \leq x \leq 0.1$)

Composition	H(applied, in Oe)	M_{Cr}(emu/g)	H_I(Oe)	θ
x = 0	500	0.083	-939.48	-43
x = 0.06	500	0.087	-1054.87	-60
x = 0.07	500	0.080	-859.77	-122

4.4.3 Field assisted memory switching

Further, magnetic switching behaviors is examined in x = 0.06 due to its high compensation temperature. Figure 4.13 shows the two distinct states of M_{FC} (under 500 Oe) as a function of time by varying the field magnitude in between 500 Oe and 1330 Oe (keeping the field direction fixed). The M_{FC} under 500Oe field cooling shows the net magnetization of the $CeCr_{1-x}Fe_xO_3$(x = 0.6) at 90K is negative. When the field is increased to 1330 Oe which is greater than the internal field value of 1054.87 Oe, the Ce^{3+}+Fe^{3+}moment flipped in field direction and achieve equal positive magnitude at 1330 Oe. When field is decreased back to

500 Oe, the internal magnetic field due to Cr^{3+} dominates over the external field due to which the Ce^{3+}+Fe^{3+} moments are flipped back to the initial state causing the net magnetization to become negative again. This kind of bipolar switching can be cycled several times and shows good reproducibility under this field induced magnetization reversal. The switching of positive and negative states of M_{FC} only by changing the magnitude of the external field endorses the application of these materials in the data storage and magnetic switching based nonvolatile magnetic memory.

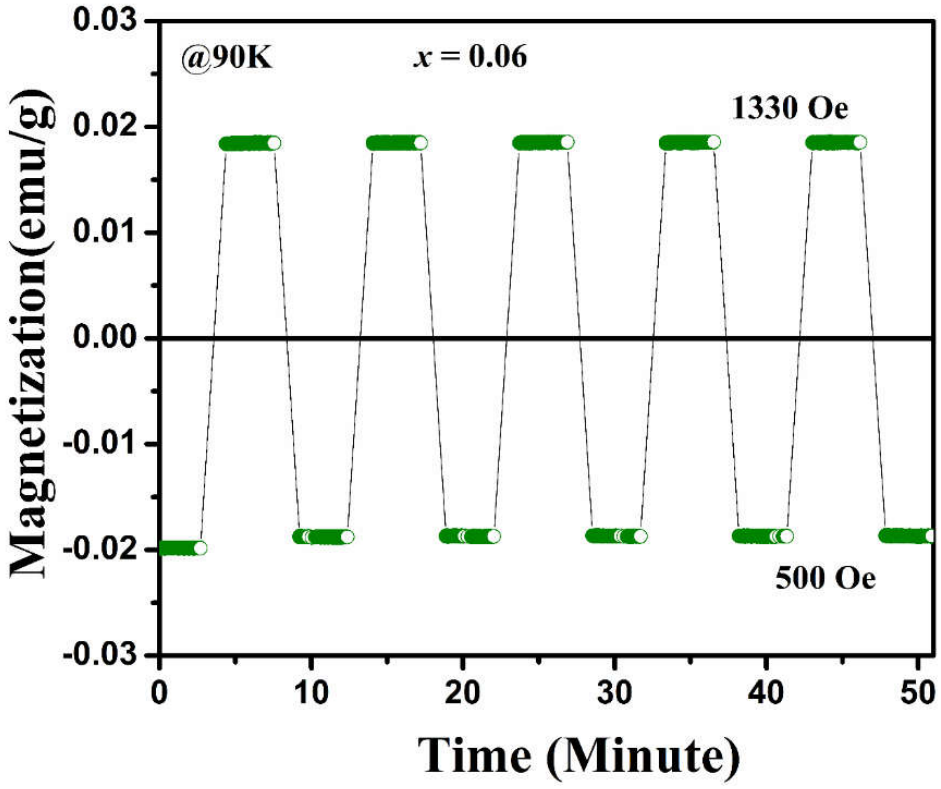

Figure 4.13 Bipolar magnetic switching behaviour in $CeCr_{1-x}Fe_xO_3$ (x = 0.06) with changing the magnitude external magnetic field in between 500 Oe and 1330 Oe in same direction.

4.5 Conclusion

In summary, we synthesized single phase pure, polycrystalline $CeCr_{1-x}Fe_xO_3$ ($0 \leq x \leq 0.1$) through solution combustion method. Phase and structure were confirmed using Rietveld refinement of XRD pattern, which revealed that the compounds were stabilized in an orthorhombic distorted perovskite structure with a *Pnma* space group(no-62). With increasing *x*, structural distortion was increased, which could be attributed to the difference in ionic radii of Fe^{3+}(0.645 Å) and Cr^{3+}(0.615 Å). The distortion in structure due to the tilting of octahedra was further supported by the change in Ag(6) mode of Raman spectra. Magnetization data revealed that with an increase in Fe^{3+} concentration, T_{N1} increased above 390 K and suppressed the Cr ordering temperature T_{N2} to 245 K. With increasing *x*, the M_{FC} were found to be positive at $x = 0.08$ which could be attributed to domination of external field over the internal field due to Cr^{3+} moment. Apart from this, the decrease in T_{comp} and increase in T_{SR} were also the consequences of external field domination over the internal field. Besides, magnetization reversal with spin reorientation, the bipolar switching behavior was also observed for $x = 0.06$. The presence of bipolar switching behavior enables these materials for the potential application in data storage as well as magnetic switching based nonvolatile magnetic memory devices.